Elsevier Editorial System(tm) for Journal of the European Ceramic Society

Manuscript Draft

Journal of European Ceramic Society 38 (2018) 403-409
doi: 10.1016/j.jeurceramsoc.2018.01.025
Submitted 17 July 2017

Manuscript Number: JECS-D-17-01291R1

Title: Method to improve the oxidation resistance of ZrB2-based ceramics for reusable space systems

Article Type: Full Length Article

Keywords: ZrB2; solid solution; Nano-structures; Oxidation; Reusable space systems.

Corresponding Author: Dr. Laura Silvestroni,

Corresponding Author's Institution: CNR

First Author: Laura Silvestroni

Order of Authors: Laura Silvestroni; Simone Failla; Irina Neshpor; Oleg Grigoriev

Abstract: UHTCs are the most suitable materials for space and hypersonic, however in service they lose their properties owing to oxidation damages. Tailoring composition and microstructure on a multiscale level may maintain structural stability in the sub-layers. Sintering of ZrB2-MoSi2 ceramics at 1900-2150°C results in microstructures characterized by partial or complete (Zr,Mo)B2 solid solutions. This has notable impacts on the performance of the composites subjected to cyclic oxidation at 1650°C. Coupled XRD, SEM and TEM analyses pointed out the formation of a unique interpenetrating microstructure, where ZrO2 micro-grains encase stable nano-sized MoB particles. This architecture manifested its suitability during repeated oxidation limiting the effect of oxygen attack to some microns thickness, due to diffused Mo which prevented turbulence and bursting phenomena on the outer glass.
This study elucidates the processing conditions that lead to the development of prominent materials for application in new generation thermal protection systems for reusable space components.

Consiglio Nazionale delle Ricerche
istec Istituto di Scienza e Tecnologia dei Materiali Ceramici

SUMMARY OF NOVEL CONCLUSIONS

Criterion Design for the Realization of Ceramic Reusable Space Systems

- Sintering of ZrB_2-$MoSi_2$ at 1900°C or 2150°C leads to the formation of partial or complete (Zr,Mo)B_2 solid solution, respectively, plus SiC and MoB.
- Different oxidized architectures form upon cyclic oxidation at 1650°C.
- (Zr,Mo)B_2 oxidizes into ZrO_2 encasing intragranular MoB nano-inclusions.
- The composites processed at 2150°C displayed outstanding oxidation behavior.
- A complete solid solution is beneficial to hamper oxidation, as it provides diffused Mo, limiting bursting phenomena on the outermost surface.

C.F. 80054330586
P.I. 02118311006
Via Granarolo, 64 I-48018 Faenza (RA)
Telefono: +39 0546 699711 - Fax +39 0546 46381
e-mail: istec@istec.cnr.it
PEC: istec@pec.cnr.it

National Research Council of Italy
istec Institute of Science and Technology for Ceramics

Faenza, January 15th 2017

ANSWER TO REFEREE'S COMMENTS

Dear Editor in Chief,

We are very grateful to the referee for his/her useful comments and suggestions on our manuscript initially entitled "Criterion Design for the Realization of Ceramic Reusable Space Systems" (JECS-D-17-01291).

All the comments have been addressed and the manuscript has been carefully revised. All the changes are marked in red in the revised file and a summary of the contents revision is reported here below.

Reviewers' comments:

Reviewer #1: The manuscript addresses the influence of the hot pressing temperature (1900 or 2150°C) on the microstructure and oxidation resistance of ZrB2-15 vol% MoSi2 composites. The information provided in the manuscript is new and contains very interesting results on the influence of the microstructure (phase composition, phase content, nature of the boride solid solution, etc) on the oxidation resistance of hot pressed ZrB2-15 vol % MoSi2 starting powders. Hot pressing at 2150°C resulted in the complete dissolution of all Mo into a (Zr,Mo)B2 solid solution with a secondary SiC phase with an excellent high temperature oxidation resistance due to the formation of a continuous silica surface layer.

The results are clearly supported by experimental evidence and are also supported by thermodynamic calculations. I therefore strongly recommend the manuscript for publication, with some minor points to be properly addressed:

- Although the title is very appealing, it does not at all inform the reader about the specific content of the paper (which type of ceramics?, which properties?). I strongly suggest to find a more dedicated title.

The title has been changed into "Method to improve the oxidation resistance of ZrB_2-based ceramics for reusable space systems"

- Did you quantify the W content in the milled starting powder?

From microstructural analysis of the sintered samples, we concluded that the W content in the milled starting powder was negligible since no discrete W-compound was found. A sentence specifying this aspect has been added in the experimental section.

- "hot pressing at CNR-ISTEC and at the installation of IPMS" does not provide any information on the specific hot presses that were used. Better to report the type and supplier of the specific hot presses used.
  We keep the distinction of the two furnace used, but added details on the hot pressing machines in the experimental section.
- p.6, line 1: "B4C is an impurity introduced during powder grinding". This statement comes as a surprise since no B4C powder grinding was reported in the experimental procedure section.
  We have revised this comment about B4C, see at the end of paragraph 3.1.
- p.6, line 32: "alien" should be "foreign" or "other"
  Changed with “foreign”.
- Fig.1: "MoB2" in the figure legend should be "MoB".
  In this case we have considered the hexagonal-MoB2 phase (and not tetragonal-MoB) supposing that all Mo could substitute Zr sites in ZrB2 lattice. Therefore we left Fig. 1 unchanged.

We hope that our manuscript in its revised form will meet the high standard for publication in the Journal of the European Ceramic Society.

Yours sincerely,

Laura Silvestroni

Journal of European Ceramic Society 38 (2018) 403-409
doi: 10.1016/j.jeurceramsoc.2018.01.025
Submitted 17 July 2017

Method to improve the oxidation resistance of ZrB_2-based ceramics for reusable space systems

Laura Silvestroni[1*], Simone Failla[1], Irina Neshpor[2], Oleg Grigoriev[2]

[1]CNR-ISTEC, National Research Council of Italy - Institute of Science and Technology for Ceramics, Via Granarolo 64, 48018 Faenza, Italy

[2]IPMS, Frantsevich Institute for Problems of Materials Sciences, 3 Krzhizhanovskoho St., 03680 Kyev, Ukraine

GRAPHICAL ABSTRACT

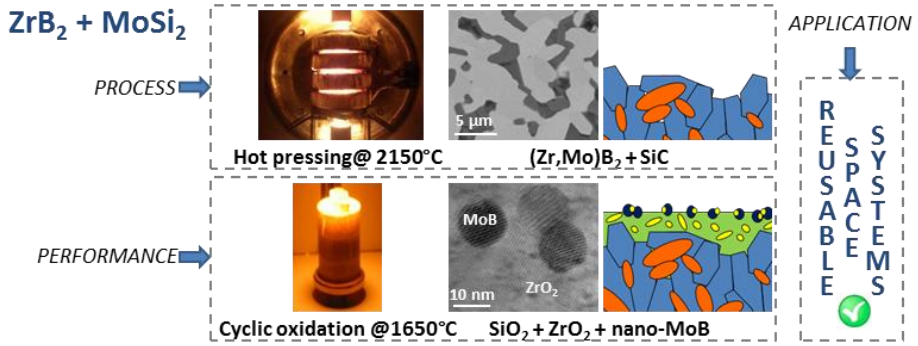

ABSTRACT

UHTCs are the most suitable materials for space and hypersonic, however in service they lose their properties owing to oxidation damages. Tailoring composition and microstructure on a multiscale level may maintain structural stability in the sub-layers. Sintering of ZrB_2-$MoSi_2$ ceramics at 1900-2150°C results in microstructures characterized by partial or complete $(Zr,Mo)B_2$ solid solutions. This has notable impacts on the performance of the composites subjected to cyclic oxidation at 1650°C. Coupled XRD, SEM and TEM analyses pointed out the formation of a unique interpenetrating microstructure, where ZrO_2 micro-grains encase stable nano-sized MoB particles. This architecture manifested its suitability during repeated oxidation limiting the effect of oxygen attack to some microns thickness, due to diffused Mo which prevented turbulence and bursting phenomena on the outer glass.

This study elucidates the processing conditions that lead to the development of prominent materials for application in new generation thermal protection systems for reusable space components.

Keywords: ZrB_2; solid solution; Nano-structures; Oxidation; Reusable space systems.

1. Introduction

One of the main technological advances required in aerospace industry is the development of reusable space systems (RSS), namely the design of components and materials that should not change their shape, size, aerodynamic and thermal protection properties as a consequence of the various physical, chemical and structural solicitations throughout the entire operation period. The benefits of RSS include the reduction of the high maintenance costs and

* Corresponding author: L. Silvestroni
Tel. +39 546 699723
Fax. +39 546 46381
e-mail. laura.silvestroni@istec.cnr.it

an increased reliability and durability, provided that they are able to tolerate some level of external damage without requiring repair [1-3].

In this perspective, the development of innovative materials for the fabrication of new generation thermal protection systems for future reusable space components would provide an answer to this demand.

The class of materials commonly termed as ultra-high temperature ceramics (UHTCs) has been indicated as the most potential candidate to constitute parts of such RSS in view of their melting point exceeding 3000°C and excellent ablation resistance as compared to SiC [3-5]. However, pure monolithic ceramics, like ZrB_2 or HfB_2, are not actually serviceable due to a series of limitations, like difficult ability to densify, poor damage tolerance and a critical oxidation resistance. In particular, the oxidation behaviour of borides has been thoroughly studied and modelled over a wide temperature range [6-7]. According to reaction (1), ZrB_2 oxidizes yielding porous ZrO_2 crystals and glassy B_2O_3. This last is liquid and partially protective up to 1000°C, but above, its volatilization leaves the porous scale fully susceptible to further oxygen attack, therefore the introduction of secondary phases that limit this and the above mentioned shortcomings is mandatory.

$$ZrB_2 + 5/2O_2 \rightarrow ZrO_{2(s)} + B_2O_{3(l/g)} \quad (1)$$

SiC phase, in form of particles, platelets or fibres, has proved to strongly enhance the thermo-mechanical properties of borides, thanks to the promotion of a refined microstructure [8-10] and triggering of toughening mechanisms [11-12], but one of the major impacts has been manifested in a notable increase of the oxidation resistance, owing to the development of a multi-layered architecture topped by a borosilicate glass upon oxidation [13-17], reaction (2). The critical aspect of SiC addition is however revealed above 1650°C, when active oxidation occurs in the subscale layers at the SiC–SiO_2 interface, owing to an unfavourable combination of low oxygen pressure and high temperature [18-19], reaction (3).

$$ZrB_2 + SiC + 4O_2 \rightarrow ZrO_{2(s)} + SiO_2{\cdot}B_2O_{3(l)} + CO_{(g)} \quad (2)$$

$$SiC + SiO_2 \rightarrow 2SiO_{(g)} + CO_{(g)} \quad (3)$$

Other phases added to expand the operation limits of ZrB_2 include transition metals, in form of borides, carbides and silicides, in view of their capability of modifying the structure and oxygen permeability of glass and crystalline phases formed, i.e. SiO_2 and ZrO_2 [20-23]. It has been ascertained that, upon sintering, the introduction of transition metals Me, where Me =Ta, Mo, W or Cr, to ZrB_2 matrices promotes the formation of $(Zr,Me)B_2$ solid solutions that epitaxially grow around the original ZrB_2 nuclei [24]. The mechanism of formation of such substructures, generally known as “core-shell”, has been attributed to partial decomposition of the sintering additive containing the transition metal [24], for example, in the case of disilicides, reaction (4-5) have been proposed:

$$MeSi_2 \rightarrow Me + 2Si_{(l)} \quad (4)$$

$$ZrB_2 + xMe \rightarrow (Zr_{1-x}Me_x)B_2 + xZr \quad (5)$$

When silicides are employed, the mass transfer is favored and assisted by a transient liquid phase formed upon interaction of the oxides that naturally cover the starting powders (6), in which both Zr and Me are partially soluble:

$$B_2O_3 + SiO_2 \rightarrow SiO_2{\cdot}B_2O_{3(l)} \quad (6)$$

Given the sharp interface between core and shell, without a diffusion gradient and often trapping Si-O-C particles [24-25], the shell structure is thought to be a consequence of re-precipitation mechanism from the liquid phase on the starting ZrB_2 cores upon cooling or when the solubility limit is achieved. Considering the same sintering temperature, ~1900°C, the amount of Me dissolved into the boride lattice mostly depends on the nature of the guest cation, found

to be 20 at% for Ta [25], below 10 at% for Mo [26] and 2 at% for W [27], however, recent results [28] have demonstrated that the solubility limit can be augmented by an increase of the sintering temperature, that accelerates the diffusion processes.

The way these core-shell structures evolve upon oxidation has been just disclosed and explained: ZrB_2 oxidizes into ZrO_2 which encases nano-inclusions whose nature depends on the oxygen and boron oxide relative partial pressures in the specific subscale [29-30]. Although those studies pointed out the neat microstructure formed and its effect on the capability to obstruct or enhance further oxygen permeation across the ZrO_2 scale, no investigation has been undertaken to study the effect of the different amounts of the same transition metal dissolved into the solid solution on the oxidation performances.

In this work, we present two ZrB_2 ceramics with initial 15 vol% $MoSi_2$ content hot pressed at two different temperatures, 1900 and 2150°C, that promoted the evolution of two dissimilar composites with different amount of Mo dissolved in the $(Zr,Mo)B_2$ solid solution. These differences were reflected on the oxidation response to cyclic tests at 1650°C in dry air. The effect of Mo content on the oxidation behavior of the two UHTCs is discussed based on microstructure evolution and thermodynamic computations.

The definition of the superiority of the mixed $(Zr,Mo)B_2$ solid solution over the pure ZrB_2 phase could provide a potential design criterion for a new paradigm of ceramics with outstanding oxidation behaviour for application in reusable space systems.

2. Experimental procedure

2.1 Materials processing

15 vol% $MoSi_2$ was added to ZrB_2 to promote its densification and the following powders were used: hexagonal ZrB_2 (Qinhuangdao Eno High-Tech Material Development Co., Ltd, China), purity>99.0%, impurities (wt%): C<0.2, Hf<0.2, Fe-0.1, mean particle size range 0.5-1.0 µm; tetragonal $MoSi_2$ (Qinhuangdao Eno High-Tech Material Development Co., Ltd, China), purity>99.9%, impurities (wt%): Ti<0.014, Mn<0.0012, Co<0.0012, Zn<0.001, Mg<0.0005, Sb<0.0003, mean particle size range 1.0-3.0 µm. Simultaneous grinding and mixing of the powders was carried out in acetone in a planetary mill for 6 hours using WC-based grinding media. No W-based compounds could be detected in the starting powder. The slurry was then dried using a rotary evaporator and finally sieved through 100 µm screen, the average powder particle size after grinding did not exceed 2.5 µm.

Sintering was performed in two different hot pressing furnaces: one at CNR-ISTEC and one at IPMS. In the first case, labeled “A” later on, a green pellet, 30 mm in diameter and 10 mm height, was shaped by uniaxial pressing and directly placed in the furnace and hot-pressed up to 1900°C in low vacuum (100 Pa) using an induction-heated graphite die with an uniaxial pressure of 30 MPa and held at the maximum temperature for 20 minutes.

In the second case, labeled “B”, an 8 mm diameter and 10 mm height pellet was sintered in a vacuum hot pressing in graphite molds. The nominal temperature on the outer surface of the mold was measured by an infrared thermometer and the actual temperature inside the mold was calculated on the basis of specific calibrating plots. The actual temperature achieved for the densification in case B was 2150°C with an applied mechanical pressure of 48 MPa, held for 10 minutes. Free cooling followed in both cases.

2.2 Oxidation test

The resistance to oxidation was studied using a bottom-loading furnace with $MoSi_2$ heating elements (Nannetti FC18, Faenza, Italy) exposing rectangular coupons 10.0 x 6.0 x 3.0 mm^3 for 15 minutes to the effect of stagnant air at 1650°C. The coupons, previously cleaned in acetone and weighed, were placed onto porous zirconia supports, previously carved to limit the contact between the two surfaces, so that the coupons touched the zirconia support only at the edges. The ceramic specimens were bottom-up loaded into the hot zone of the furnace when the target temperature was achieved, elapsed 15 minutes and rapidly down-loaded from the hot chamber and let quench in air. This oxidation cycle was repeated 3 times for a total duration of 45 minutes at 1650°C.

2.3 Materials characterization

The final density of the two pellets was measured by the Archimedes' method in distilled water.

Crystalline phases of the as-sintered and oxidized ceramics were identified by X-ray diffraction (XRD, mod. D8 Advance - Bruker, Germany) with Cu Kα radiation, step size of 0.02 and 0.5 s counting rate in the 20-130° 2-Theta range.

The microstructure before and after oxidation was analyzed on fractured and polished cross-sections by field-emission scanning electron microscopy (FESEM, mod. ΣIGMA, ZEISS NTS Gmbh, Germany) coupled to an energy dispersive X-ray micro-analyzer (EDS, mod. INCA Energy 300, Oxford Instruments, UK). Key microstructural features like residual porosity, mean grain size and volumetric content of the secondary phases were evaluated from FESEM micrographs elaborated with the support of the commercial software package Image Pro Plus (v.7, Media Cybernetics, USA).

The sample for TEM analyses was prepared by cutting a disc from sample A upon oxidation. The disc was mechanically ground down to about 20 μm and then further ion beam thinned until incipient perforations were observed by optical microscope. Local phase analysis was performed using a transmission electron microscope (TEM, JEOL JEM 2100F) operating at a nominal voltage of 200 kV and equipped with an energy-dispersive X-ray system (EDS, mod. INCA Energy 300, Oxford instruments, UK). Electron diffraction patterns identification was carried out through the software tool developed for Digital Micrograph [31].

Thermodynamics and phase stability diagrams were computed by means of the commercial package HSC Chemistry v. 6.12 (Outokumpu research Oy, Pori, Finland).

3. Results and Discussion

3.1 As-sintered microstructure

Table I summarizes the main processing conditions and resulting microstructural features of the two ZrB_2-$MoSi_2$ ceramics that will be discussed in the following.

X-ray diffraction analysis revealed that in material A the boride peaks result split, demonstrating that the nominally pure ZrB_2 is still present together with a new $(Zr,Mo)B_2$ solid solution with contracted unit cell parameters due to the substitution of Mo, with smaller ionic radius (1.36 Å nm), into Zr sites, with larger ionic radius (1.60 Å), in agreement with previous studies on borides sintered in presence of transition metal silicides or carbides [24]. On the contrary, in material B, all peaks corresponding to ZrB_2 are shifted to higher 2-Theta angles indicating the formation of one single solid solution.

A zoomed portion of the x-ray diffraction patterns of the as sintered ceramics displaying the peaks splitting or shift is shown in Fig. 1. The table inset reports the lattice constants of the reference pure diboride phases, ZrB_2 and MoB_2, together with those of the two $(Zr,Mo)B_2$ solid solutions. An estimation of the Mo at% in each solid solution by Vegard's rule led to a $(Zr_{0.98}Mo_{0.02})B_2$ phase in material A and $(Zr_{0.88}Mo_{0.12})B_2$ in material B, in agreement with the different sintering temperatures experienced. The composition of these new solid solution is just indicative, since peak shifting could be due also to residual stresses arose in the sintered bulks upon cooling, due to the different coefficient of thermal mismatch of the composing phases. The main thing to notice here is the notably different Mo content in the two solid solutions passing from a sintering temperature of 1900°C to 2150°C, ~2 at% compared to ~12 at%, respectively. Secondary phases include hexagonal SiC and traces of tetragonal MoB, more pronounced in material A. In none of the ceramics, residual $MoSi_2$ was detected.

A - Images of the microstructure of material A are displayed in Fig. 2a-c. Fig. 2a shows an overall view of the polished section: no major defects or residual porosity can be observed, two secondary phases can be identified: a dark contrasted one, SiC with SiO_2 pockets at the edges, and a bright one in the same amount, with irregular shape and low dihedral angles, Fig. 2b,c and Table I. EDS pointed out this to be MoB with W traces, owing to impurity take up during milling. The formation of SiC and SiO_2 can be explained following reaction (7), which also leaves notable amount of free Mo:

$$MoSi_2 + CO_{2(g)} \rightarrow SiC + SiO_{2(l)} + Mo \qquad (7)$$

MoB phase is commonly observed in the ZrB_2-$MoSi_2$ system [24,28] and it derives from the reaction between $MoSi_2$ and the oxides that naturally cover the starting ZrB_2 powders [32], reaction (8):

$$2MoSi_2 + B_2O_3 + 5/3CO_{(g)} \rightarrow 2MoB_{(s)} + 5/3SiC + 7/3SiO_{2(l)} \qquad (8)$$

The matrix grains are rounded with average dimensions of 1.9 μm, different grey levels are due to different grains orientation. Fig. 3a-b discloses the morphology of the matrix: the core is ZrB_2, whilst the outer darker region, the rim, is ZrB_2 containing 6 at% of Mo, as the EDS spectra demonstrates with the tiny peak at 2.3 keV. The discrepancy with the Mo amount estimated by X-ray diffraction, 2 at%, is certainly due to the low quantity dissolved in the solid solution of material A, within the experimental error of the diffractometer. Given the precision of the two techniques, we consider the value obtained by EDS more reliable.

Occasionally residual $MoSi_2$ is found, but its amount can be negligible, below 1 vol%. The amounts of the secondary phases formed, MoB and SiC, are in agreement with the complete decomposition of $MoSi_2$ according to reaction (8).

B - An overview of the microstructure of material B is displayed in the SEM images of Fig. 2d-f, the grey phase is the newly formed $(Zr,Mo)B_2$ compound and the dark phase is a combination of SiC, B_4C and silica-based glass. The matrix grains are slightly elongated, with the longest axis between 5-7 μm and aspect around 1.8. EDS elemental mapping shows that Mo is homogeneously dispersed in the boride matrix and its distribution is not overlapped with that of Si, Fig. 3c, confirming complete $MoSi_2$ dissociation. The amount of Mo dissolved in the solid solution is now 12 at%, Fig. 3d, in perfect agreement with the estimation from the x-ray diffraction pattern. The volume fraction of the dark phase is notably in higher amount and different shape as compared to material A, around 21 vol%. SiC grains, with maximum length of 3-5 μm, are characterized by elongated shape with aspect ratio around 3 and their shape indicates the presence of only the α polytype. Its relative amount is estimated to be around 15 vol% by image analysis, whilst the residual 6 vol%, with irregular profiled shape, is mostly SiO_2 pockets and B_4C, Fig. 2b. SiO_2 is a residual of

$MoSi_2$ dissociation, whilst B_4C is a product formed upon sintering owing to the high carbon mobility at the elevate temperatures during hot pressing.

3.2 Microstructure upon oxidation

A photo of the oxidized samples after 3 cycles of 15 minutes at 1650°C is reported in the inset of Fig. 4. The aspect of the UHTCs after three cycles did not notably vary in case B, where just some shiny covering can be seen due to glass formation, whilst bubbling and little whitening is observed for material A. However, no delamination or spallation of the external oxide occurred in any material. The specific weight gain was in both cases negligible, higher after the first cycle, 0.2-0.3%/cm^2, and stable after the second and third ones, below 0.1%/cm^2.

The x-ray diffraction patterns recorded on the surface of the specimens after cyclic oxidation are reported in Fig. 4. As expected, the main crystalline phase is monoclinic ZrO_2 with traces of tetragonal MoB in material A. Astonishingly, in material B, ZrB_2 is retained as main crystalline phase and only little traces of monoclinic ZrO_2 and MoB are found.

SEM images of the external surfaces reported in Fig. 5, show that both materials are covered by a continuous silica-based glass with crystalline bright precipitates. Some bubbling phenomena occurred, especially in sample A.
The surface of material A is in general rougher and no Mo is detected within the white crystalline precipitates, Fig. 5a,b. This can be due to the low amount of Mo dissolved in the solid solution of material A, resulting in small and few Mo-based inclusions. In addition, ZrO_2 aggregates located in larger SiO_2-rich area with different contrast glass surrounding the aggregates are commonly found and can be associated to the convection cells described in [33].
The aspect of the outer surface of material B is smooth and regular, Fig. 5c. Silica glass does not contain foreign cations, nor Zr, nor Mo, Fig. 5d. Higher magnification images of the bright precipitates in material B evidence the formation of tiny bright rounded particles homogeneously dispersed on the surface of ZrO_2 grains, Fig. 5e-f. These contain Mo-B and have variable diameter between 50 and 180 nm.

The cross sections of the oxidized samples are reported in the SEM images of Fig. 6. As first observation, it can be remarked the excellent oxidation resistance of material B, where less than 20 µm of outer SiO_2 glassy phase effectively protected the bulk, as no ZrO_2 layer can be delineated, Fig. 6a,c.

Material A allowed the oxidation of a thicker portion of material, ~60 µm. Similar to other ZrB_2-based ceramics, material A shows a multilayered architecture. Two main scales and two interfaces of the volume interested by the oxidation attack are identified, Fig. 6b. A continuous surface silica scale, labeled *SZ*, about 20 µm thick embeds ZrO_2 grains and agglomerates, Fig. 6b. Moving towards the ceramic core, a 40 µm thick and dense ZrO_2-based layer, *ZSM,* containing $MoSi_2$ oxidation products, namely SiO_2 and MoB, is found before the un-oxidized bulk. It can be noticed that the repeated oxidation progressively induced the migration of silica close to the upper surface, indicating that at this temperature silica is very fluid. In addition, Fig. 6b displays the morphology of MoB and SiO_2 phases adjacent to each other and well dispersed in the *ZSM* layer. A magnified picture of ZrO_2 grains at the *SZ/ZSM* interface in the inset of Fig. 6b evidences that silica glass fills the interstitials among ZrO_2 growing grains and MoB large particles are located up to the *SZ/ZSM* interface, suggesting a critical variation of partial pressure at this depth. Furthermore, an intra-granular nano-sized structure, characterized by bright contrasts and rounded shape, is found encased and decorating ZrO_2 grains. TEM investigations allowed a more precise definition of the nature of such inclusions. Fig. 7a displays the overall appearance of ZrO_2 grains encasing dispersed particles and connected by dislocations. In Fig.7b

the lamella growing planes associated to the tetragonal-to-monoclinic phase transformation of ZrO_2 [34] are well visible, whilst Fig. 7c-d show high resolution images of MoB particles with the corresponding diffraction pattern and EDS spectra. Given the tiny size of the inclusions, 10-20 nm, both signals about crystallinity and chemistry are overlapped to that of ZrO_2, Fig. 7e-f. Similar intra-granular nanostructured morphology was observed upon oxidation of $(Zr,W)B_2$ and $(Zr,Ta)B_2$ solid solutions [29-30].

In material B, at the silica/bulk interface, MoB phase is systematically found immersed in the glass and in form of nano-aggregates and platelets, Fig. 6e. Underneath, the $(Zr,Mo)B_2$ solid solution and SiC remained unaffected by oxygen attack.

3.3 Sintering behavior

From the microstructures just presented, Table I, and from previous investigations on this system [24], a general sintering mechanism can be drawn. A schematic of the microstructure evolution upon sintering and after oxidation of the two ceramics is sketched in Fig. 8.

$MoSi_2$ is not stable at high temperature in vacuum and tends to dissociate into Si and Mo [24]. The first is liquid above 1400°C, which is close to the temperature at which shrinkage is recorded and runs along the boride particles cleaning them from the covering oxides, ZrO_2 and B_2O_3, thus making the boride powder more reactive to sinter. Mo is then dissolved in a Si-Mo-Zr-B-O transient liquid phase which favors densification [35]. When the sintering is performed at 1900°C, upon cooling, an epitaxial $(Zr,Mo)B_2$ solid solution precipitates on the original ZrB_2 nuclei, MoB crystallizes with residual SiO_2 glassy phase. As a consequence of the high carbon mobility at the sintering temperatures, from dies and rams, silica is carbo-reduced to SiC phase.

In material B, at increased sintering temperature, 2150°C, $MoSi_2$ is completely dissociated as well and Mo is fully encased into a new single $(Zr,Mo)B_2$ solid composing the matrix. MoB is not present, since residual oxide phases are reduced owing to the increased carbon diffusivity above 2000°C. In addition, SiC has a platelet-like shape, implying the presence of only α polytype.

The observation of only SiC in material B, whilst a combination of equal volume fraction of SiC and MoB in material A suggests that at low temperature, case A, reaction (8) is more favorable, whilst at higher temperature, case B, reaction (7) prevails, in agreement with thermodynamic computations. The plot in Fig. 9a shows the free Gibbs energy calculated at atmospheric pressure[†] as a function of the sintering temperature for reactions (7) and (8) and, indeed, there is an inversion of the favorability of occurrence at around 1600°C. It has to be underlined that both hot pressings were performed in vacuum, therefore the discrepancy between the actual and calculated cross temperature could be attributed to a different pressure inside the hot pressing chamber.

3.4 Oxidation behavior

In order to correlate the different oxidation behaviors of the two nominal identical composites, one has to keep in mind the main microstructural differences resulted from two different sintering temperatures, 1900°C for material A and 2150°C for material B, Fig. 8. Therefore, the discussion will focus on the effect of three major aspects: i) the type and amount of secondary phases, ii) the chemistry of the matrix and iii) the grain size of the matrix.

[†] The software used, HSC Chemistry v. 6.12, allows this type of calculations only at atmospheric pressure.

i) The first issue regards the secondary phase. $MoSi_2$ in both cases is completely dissociated upon densification and not detected any more in the microstructure, nor by XRD nor by SEM-EDS. However, due to the different sintering temperatures, 7 vol% of MoB and 7 vol% of SiC are found in ceramic A, whilst 15 vol% of SiC is present in material B. What follows from different type and amount of secondary phases is the quantity of liquid SiO_2 phase produced upon oxidation, following reactions (2) or (9), and also the composition of the formed glass, that may have different viscosity, influenced by a different cations content, owing to the capturing of Mo from reaction (10):

$$SiC + 3/2O_2 \rightarrow SiO_{2(l)} + CO_{(g)} \quad (9)$$

$$MoB + 2O_2 \rightarrow MoO_{3(g)} + B_2O_{3(l/g)} \quad (10)$$

The free Gibbs energy of reactions (9) and (10) calculated at 1650°C, atmospheric pressure and normalized with respect to the moles of oxygen is -126 and -121 kcal, respectively, indicates that SiC is the phase oxidizing first and able to form a continuous protective silica layer on the surface. In this respect, material B will display a better oxidation protection as compared to A, firstly due to higher amount of SiC.

Given the lack of data on viscosity of borosilicate glass containing Zr and Mo dissolved and in the temperature of interest, considerations on the glass are done just in a speculative way. B_2O_3 is highly volatile at 1650°C and it is therefore supposed to immediately evaporate once it achieves the surface. As a matter of fact, chemical analysis performed on the outer glass by SEM-EDS did not evidence substantial compositional differences between material A and B, suggesting either a poor Mo solubility into silica and/or a rapid evaporation of MoO_3 at 1650°C. It has been reported that convection cells on the surface are formed from ZrO_2 precipitates from a boria–silica–zirconia oxide liquid that forms upon oxidation above 1550°C, and glass with larger SiO_2/B_2O_3 ratio will dissolve less ZrO_2 [34]. Therefore, higher SiC-containing ZrB_2-composites, like material B, present less dissolved ZrO_2 because they have more SiO_2 available, which results in a smaller amount of precipitated ZrO_2 and fewer convection cells.

The more pronounced bubbling activity observed on the surface of material A, Fig. 5a, indicates the formation of more or just more localized gaseous species in the subsurface layer, these may include B_2O_3, SiO and MoO_3. However, boron oxide amount is equally present in the two materials given the same boride matrix; $SiO_{(g)}$ forms at the SiC/SiO_2 interface at oxygen partial pressure below 10^{-11} Pa, i.e. lower than the actual region right underneath the silica shield where bubbling is observed [36]; at last gas formation close to the surface is likely to be attributed to MoO_3, which is reported to vaporize accompanied by “important gas turbulence” [37]. Since the initial Mo-amount is the same in the two materials, the most probable hypothesis is related to a different distribution of Mo-cations and hence of volatile Mo-oxides: in A it is present both as discrete phase, MoB, and distributed throughout the boride matrix within the solid solution, instead in B, Mo is just homogeneously encased into the boride matrix. Therefore, we suppose that where MoB large aggregates are present in high concentration close to the surface, higher amount of localized MoO_3 will be developed, thus provoking bursting in silica glass.

ii) Concerning the matrix, in the first case pure ZrB_2 is still present together with a $(Zr,Mo)B_2$ solid solution containing almost halved amount of atomic Mo as compared to the solid solution formed in material B, where it is a continuous and homogeneous matrix. The main implication of these differences regards the distribution of Mo oxidation products within the boride matrix. The matter if pure ZrB_2 is more oxidation resistant than Mo-doped ZrB_2 cannot be solved by thermodynamics, due to the lack of fundamental input data in commercial software of such mixed compounds, therefore it will be treated in a speculative way.

SEM-EDS analysis confirmed by TEM investigations demonstrated that the oxidation of the solid solution results in ZrO_2 encasing MoB nano-inclusions, Fig. 7, following an overall reaction path that can be summarized in (11):

$$(Zr_{1-x}Mo_x)B_2 + (5/2-7/4x)O_2 \rightarrow (1-x)ZrO_2 + xMoB + (1-x/2)B_2O_3 \quad (11)$$

The oxidation of the boride phases releases significant amounts of B_2O_3, which is gaseous at 1650°C and therefore plays a fundamental role in changing the overall partial pressures and in the formation of condensed phases in the sublayers. In this respect, the complex reactivity environment in the subsurface scales, at a lower oxygen partial pressure than on the outermost surface, can be represented through the phase stability diagrams calculated at 1650°C for the Zr-B-O and Mo-B-O systems varying the oxygen and boron oxide partial pressure, Fig. 9b,c. Looking at the shaded areas in the plots of Fig. 9b,c, we notice that at 1650°C, from 10^{-10} to 10^{-13} atm of oxygen partial pressures, the stable condensed phases are ZrO_2 in the Zr-B-O system and MoB and Mo in the Mo-B-O system. This indicates that ZrO_2 is thermodynamically more stable than Mo-oxides, so that the limited amount of oxygen diffusing through the oxide scale is preferentially captured by the Zr-containing phases, and will leave solid MoB/Mo un-oxidized. However, moving to higher oxygen partial pressures, Mo is unavoidably lost by sublimation as oxide [37]. This explains why MoB is detected only up to the *SZ/ZSM* interface and not anymore in *SZ* layer, see Fig. 6b.

According to the microstructure analysis and available thermodynamics, we conclude that a material containing Mo homogeneously distributed in a boride matrix, i.e. fully dissolved in the $(Zr,Mo)B_2$ solid solution, will generate a smoother oxidized surface due to limited bubbling phenomena that intensify oxygen penetration through the bulk.

The choice of cation to be dissolved into the boride matrix has a paramount importance. As long as the nano-inclusions nestled into ZrO_2 are located at oxygen partial pressure below 10^{-10}-10^{-12} Pa, they are stable as solid compounds. However, above this pressure threshold one has to consider the oxide that they will form and in which state this will be. For example, according to studies performed on the ZrB_2 containing Ta or W [29-30], it resulted well evident that the evolution of the encased particles to solid Ta_2O_5, accompanied by a large volume expansion, or to gaseous WO_x, respectively, was fatal for the disruption or preservation of the ZrO_2 solid structure, respectively.

iii) Finally, the grain size of the two materials is notably different, around 2 µm for the material sintered at the lowest temperature and around 5-7 µm for the material sintered at the highest temperature. This factor may have an impact on the oxygen diffusion along grain boundaries. Although the ZrO_2-based scale in material A looks compact, it is noticeable that silica veins regularly run along the grain boundary. The oxygen diffusion across amorphous silica, that likely contains dissolved boron too [38] is higher than the diffusion across crystalline ZrO_2 [39-40]. Therefore also this feature may have contributed to the higher oxidation degree of material A.

4. Conclusions

A ZrB_2 - 15 vol% $MoSi_2$ powder mixture was sintered to full density at two temperatures, 1900 and 2150°C, resulting in notably different microstructural features. The lowest temperature induced the formation of core-shell grains in the boride matrix, where the core is ZrB_2 and the shell a $(Zr_{0.94}Mo_{0.06})B_2$ solid solution and, of the initial $MoSi_2$ content, 7 vol% of MoB phase was found together with 7 vol% of SiC as a consequence of the silicide dissociation and reaction within reducing atmosphere. At higher temperature, the matrix evolved instead into a continuous solid solution with higher Mo content dissolved in the solid solution, $(Zr_{0.88}Mo_{0.12})B_2$, and about 15 vol% of SiC phase with platelet shape.

The oxidation resistance at 1650°C for 15 minutes and repeated three times evidenced the superior performances of the material sintered at 2150°C owing to a combination of favorable factors:

i) higher SiC content, able to provide an outermost stable silica-based layer;

ii) a diffused Mo supply from the solid solution, which evolves into an architecture organized on a multi-scale level where ZrO_2 grains encase solid and stable MoB nano-inclusions and limit turbulence or bursting phenomena on the surface glass due to development of volatile MoO_3;

iii) a coarser grain size that notably reduces the oxygen permeability along the grain boundaries through the borosilicate glassy phase.

This study outlined the importance of an appropriate processing route to obtain ceramic composites suitable for application in reusable space systems, thus opening a new path to the design of materials with exceptional oxidation performances at ultra-high temperatures and with long-lasting usability in service.

Acknowledgements

Part of the research leading to these results has received funding from the European Community's Seventh Framework Programme (FP7/2011-2014) under grant agreement LIGHT-TPS No. 607182. D. Dalle Fabbriche is acknowledged for oxidation tests.

References

1. A. Gülhan, RESPACE – Key Technologies for Reusable Space Systems, Springer-Verlag, Berlin Heidelberg, 2008, DOI 10.1007/978-3-540-77819-6.
2. S. Cook, U. Hueter, NASA's integrated space transportation plan—3rd generation reusable launch vehicle technology update, Acta Astronaut 53 (2003) 719–728.
3. L. Kaufman, E. Clougherty, Investigation of boride compounds for very high temperature applications, Technical Report RTD-TDR-63-4096: part 2. WPAFB, OH: Air Force Research Laboratory, February 1965.
4. S.R. Levine, E.J. Opila, M.C. Halbig, J.D. Kiser, M. Singh, J.A. Salem, Evaluation of Ultra-High temperature ceramics for aero-propulsion use, J. Europ. Ceram. Soc. 22 (2002) 2757–2767.
5. W.G. Fahrenholtz, E.J. Wuchina, W.E. Lee, Y. Zhou, Ultra-High Temperature Ceramics: Materials for Extreme Environment Applications, Wiley & Sons Inc., Hoboken, New Jersey, 2014.
6. T.A. Parthasarathy, R.A. Rapp, M.M. Opeka, R.J. Kerans, A model for transitions in oxidation regimes of ZrB_2, Mater. Sci. Forum, 595–598 (2008) 823–832.
7. T.A. Parthasarathy, R.A. Rapp, M.M. Opeka, R.J. Kerans, A model for the oxidation of ZrB_2, HfB_2 and TiB_2, Acta Mater. 55 (2007) 5999–6010.
8. F. Monteverde, Beneficial effects of an ultra-fine α-SiC incorporation on the sinterability and mechanical properties of ZrB_2, App. Physics A: Mater. Sci. & Process. 82 (2006) 329-337.
9. C. Hu, Y. Sakka, H. Tanaka, T. Nishimura, S. Guo, S. Grasso, Microstructure and properties of ZrB_2-SiC composites prepared by spark plasma sintering using $TaSi_2$ as sintering additive, J. Europ. Ceram. Soc. 30 (2010) 2625-2631.
10. M. Mallik, S. Roy, K.K. Ray, R. Mitra, "Effect of SiC content, additives and process parameters on densification and structure-property relations of pressureless sintered ZrB_2-SiC composites", Ceramics International 39, 2915-2932 (2013).

11. D. Sciti, L. Silvestroni, Processing, sintering and oxidation behavior of SiC fibres reinforced composites ZrB_2 composites, Europ. Ceram. Soc. 32 (2012) 1933-1940.
12. D. Sciti, L. Silvestroni, V. Medri, S. Guicciardi, Pressureless sintered in-situ toughened ZrB_2-SiC ceramics, Europ. Ceram. Soc. 31 (2011) 2145-2153.
13. C.M. Carney, P. Mogilevsky, T.A. Parthasarathy, Oxidation behavior of zirconium diboride silicon carbide produced by the spark plasma sintering method, J. Am. Ceram. Soc. 92 (2009) 2046–2052.
14. X.H. Zhang, P. Hu, J.C. Han, Structure evolution of ZrB_2–SiC during the oxidation in air, J. Mater. Res. 23 (2008) 1961–1972.
15. W.G. Fahrenholtz, Thermodynamic analysis of ZrB_2–SiC oxidation: formation of a SiC depleted region, J. Am. Ceram. Soc. 90 (2007) 143–148.
16. P. Hu, W. Guolin, Z. Wang, Oxidation mechanism and resistance of ZrB_2–SiC composites, Corros. Sci. 51 (2009) 2724–2732.
17. K. Shugart, E. Opila, SiC Depletion in ZrB_2–30 vol% SiC at Ultrahigh Temperatures, J. Am. Ceram. Soc. 98 (2015) 1673–1683.
18. N.S. Jacobson, D.L. Myers, Active oxidation of SiC, Oxid. Metals, 75 (2011) 1-25.
19. B. Harder, N. Jacobson, D. Myers, Oxidation transitions for SiC- Part II: Passive to active oxidation, J. Am. Ceram. Soc. 96 (2013) 606-612.
20. P. Hu, X.H. Zhang, J.C. Han, X.G. Luo, S.Y. Du, Effect of Various Additives on the Oxidation Behavior of ZrB_2-Based Ultra-High-Temperature Ceramics at 1800°C, J. Am. Ceram. Soc. 93 (2010) 345–349.
21. L. Silvestroni, G. Meriggi, D. Sciti, Oxidation behavior of ZrB_2 composites doped with various transition metal silicides, Corros. Sci. 83 (2014) 281–291.
22. H. Pastor, R. Meyer, An Investigation of the effect of additions of metal silicides on titanium and zirconium borides from the point of view of their sintering behavior and their resistance to oxidation at high temperature, Rev. Int. Htes Temp. Refract. 2 (1974) 41–54.
23. C.M. Carney, T.A. Parthasarathy, M.K. Cinibulk, Oxidation resistance of hafnium diboride ceramics with additions of silicon carbide and tungsten boride or tungsten carbide, J. Am. Ceram. Soc. 94 (2011) 2600–2607.
24. D. Sciti, L. Silvestroni, V. Medri, F. Monteverde, Sintering and densification of ultra-high temperature ceramics, in: W.G. Fahrenholtz, E.J. Wuchina, W.E. Lee, Y. Zhou (Eds.), Ultra-High Temperature Ceramics: Materials for Extreme Environment Applications, Wiley & Sons Inc., Hoboken, New Jersey, 2014, pp. 112-143.
25. L. Silvestroni, D. Sciti, Densification of ZrB_2–$TaSi_2$ and HfB_2–$TaSi_2$ Ultra-High-Temperature Ceramic Composites, J. Am. Ceram. Soc. 94 (2011) 1920-1930.
26. P.S. Kislyi, M.A. Kuzenkova, Gas-impermeable protective thermocouple sheaths from zirconium boride, Powder Metall. Met. Ceram. 4 (1965) 23-26.
27. L. Silvestroni, D. Sciti, TEM analysis, mechanical characterization and oxidation resistance of a highly refractory ZrB_2-composite, J. Alloys and Compounds B, 602 (2014) 346-355.
28. R. Groshmeyer, Processing, Microstructure, and Mechanical Properties of Zirconium Diboride-Molybdenum Disilicide Ceramics and Dual Composite Architectures, PhD Dissertation, Missouri University of Science and Technology, 2017.

29. L. Silvestroni, D. Sciti, F. Monteverde, K. Stricker, H-J. Kleebe, Microstructure evolution of a W-doped ZrB_2 ceramic upon high-temperature oxidation, J. Am. Ceram. Soc. 100 (2017) 1760-1772.
30. L. Silvestroni, H-J. Kleebe, Critical oxidation behavior of Ta-containing ZrB_2 composites in the 1500-1650°C temperature range, J. Europ. Ceram. Soc. 37 (2017) 1899–1908.
31. D.R.G. Mitchell, DiffTools: Software Tools for Electron Diffraction in Digital Micrograph, Micr. Res. and Technique, 71 (2008) 588-593.
32. W.A. Zdaniewski, N.L. Brungard, X-ray photoelectron spectroscopy studies of metallic diborides, J. Am. Ceram. Soc. **75** (1992) 2849-2856.
33. S.N. Karlsdottir, J.W. Halloran, Oxidation of ZrB_2–SiC: Influence of SiC Content on Solid and Liquid Oxide Phase Formation, J. Am. Ceram. Soc., 92 (2009) 481–486.
34. P. M. Kelly, L. R. F. Rose, 'The Martensitic Transformation in Ceramics—Its Role in Transformation Toughening, Prog. Mater. Sci. 47 (2002) 463–557.
35. L. Silvestroni, H-J. Kleebe, S. Lauterbach, M. Müller, D. Sciti, Transmission Electron Microscopy on Zr- and Hf-borides with $MoSi_2$ addition: Densification Mechanisms, J. Mater. Res. 25 (2010) 828-834.
36. W.G. Fahrenholtz, Thermodynamic Analysis of ZrB_2–SiC Oxidation: Formation of a SiC-Depleted Region, J. Am. Ceram. Soc. 90 (2007) 143–148.
37. E.A. Gulbransen, K.F. Andrew, F.A. Brassart, Oxidation of Molybdenum 550° to 1700°C, J. Electrochem. Soc. 110 (1963) 952-959.
38. K. Shugart, S. Liu, F. Craven, E. Opila, Determination of retained B_2O_3 content in ZrB_2-30 vol% SiC oxide scales, J. Am. Ceram. Soc. 98 (2015) 287–295.
39. E.L. Courtright, J.T. Prater, C.H. Henager, E.N. Greenwell, Oxygen permeability for selected ceramic oxides in the range 1200°C-1700°C, WL-TR-91-4006, Final report September 1987- May 1989, (May 14, 1991).
40. A. Madeyski, W. W. Smeltzer, Oxygen Diffusion in Monoclinic Zirconia, Mater. Res. Bull. 3 (1968) 369-376.

Tables

Material	Sintering, °C, MPa, min	porosity, %	Phases upon sintering, vol%	Mo dissolved into ZrB_2, at%	Matrix m.g.s.
A	1900, 30, 20	<1	(Zr,Mo)B_2, ZrB_2, 7 MoB, 7 SiC, 2SiO_2	6	1.9±0.7
B	2150, 48, 10	<1	(Zr,Mo)B_2, 15 SiC, 3 B_4C, 3 SiO_2	12	4.1±1.5

Table I: Summary of the processing conditions and microstructural features upon sintering of the two ZrB_2-15 vol% $MoSi_2$ composites.

Figure

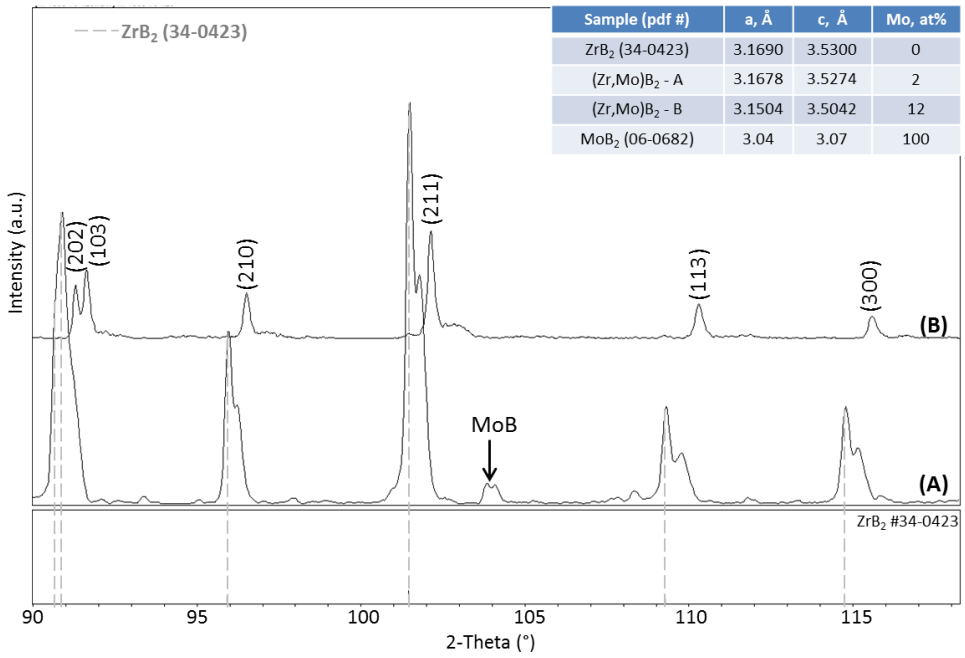

Sample (pdf #)	a, Å	c, Å	Mo, at%
ZrB_2 (34-0423)	3.1690	3.5300	0
$(Zr,Mo)B_2$ - A	3.1678	3.5274	2
$(Zr,Mo)B_2$ - B	3.1504	3.5042	12
MoB_2 (06-0682)	3.04	3.07	100

Fig. 1: *X-ray diffraction patterns of materials A and B showing peaks splitting in the first and peaks shift in the second one. The table inset lists the calculated lattice parameters for the two solid solutions and the amount of Mo dissolved, as estimated from Vegard's rule.*

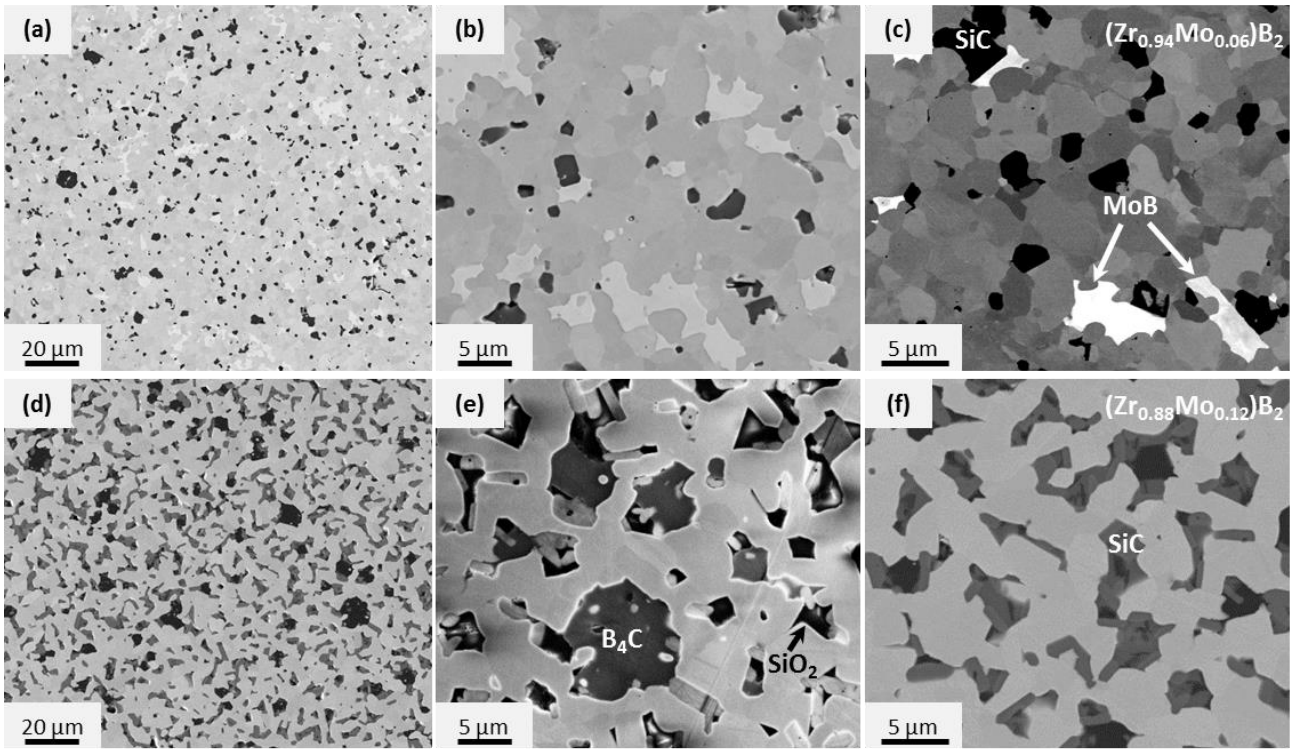

Fig. 2: *SEM images showing the microstructure of material A (a-c) and B (d-f).*

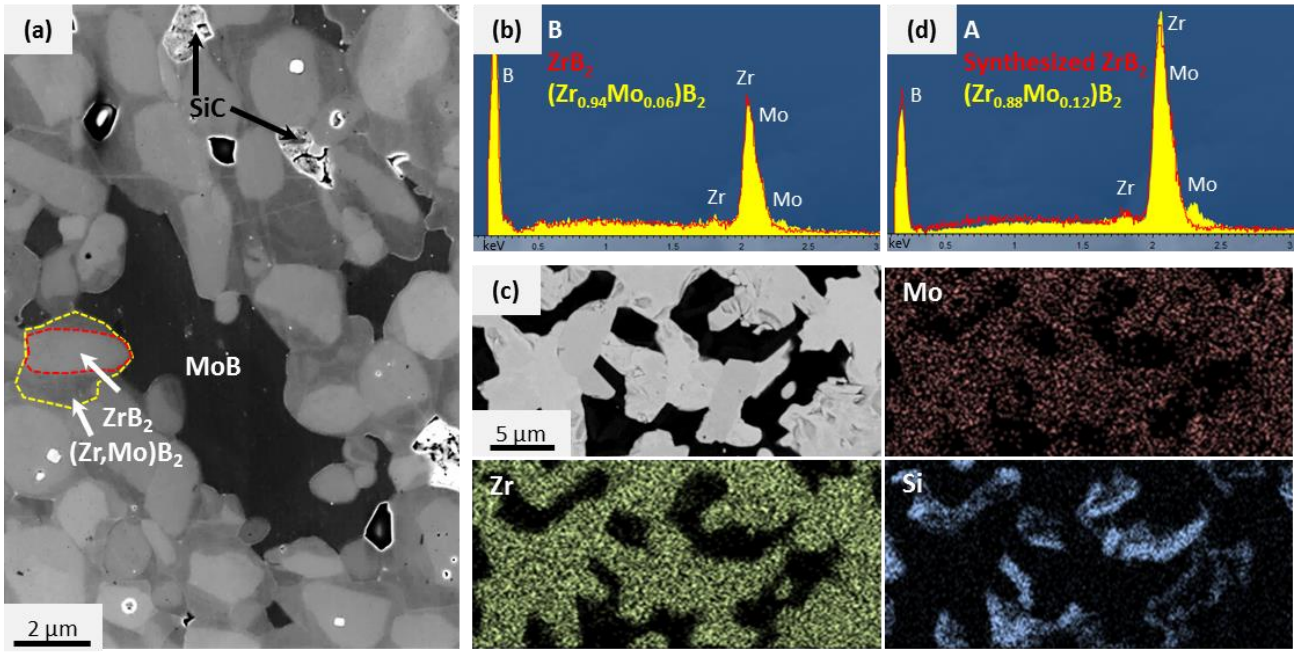

Fig. 3: *a) SEM image showing microstructural details in material A with the corresponding b) EDS spectra of core and rim phases. c) SEM image of material B with elemental distribution of Zr, Mo and Si with d) EDS spectra of the* $(Zr,Mo)B_2$ *solid solition superimposed to that of pure* ZrB_2*.*

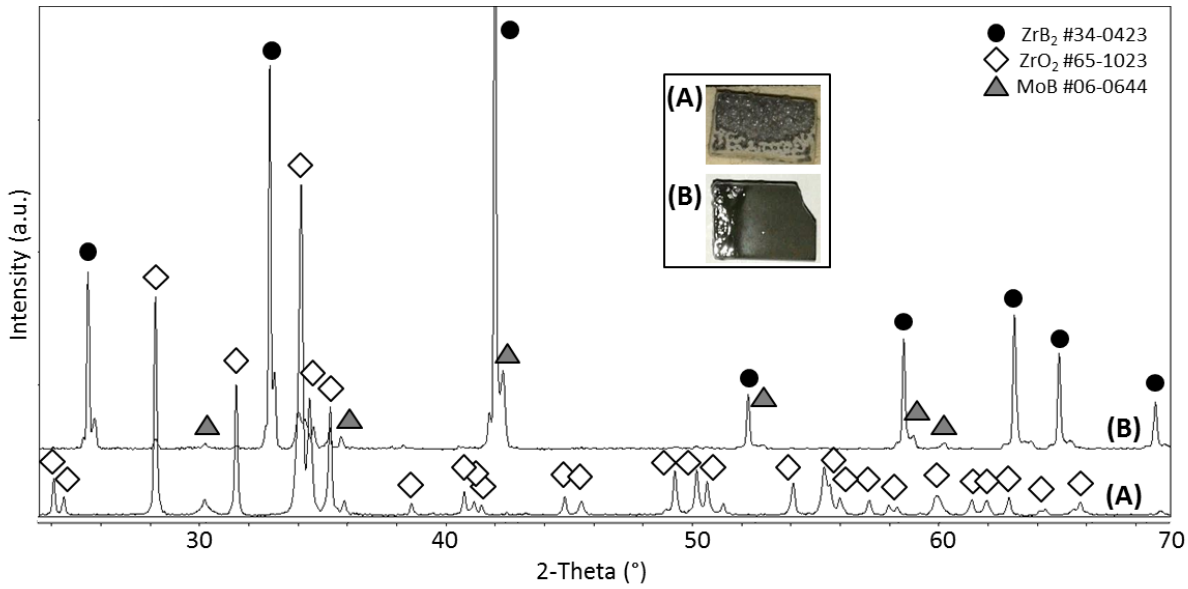

Fig. 4: *X-ray diffraction patterns of materials A and B upon cyclic oxidation showing the boride as main phase in the first and the oxide in the second one. The inset shows photos of the ceramics after the 3 oxidation cycles at 1650°C.*

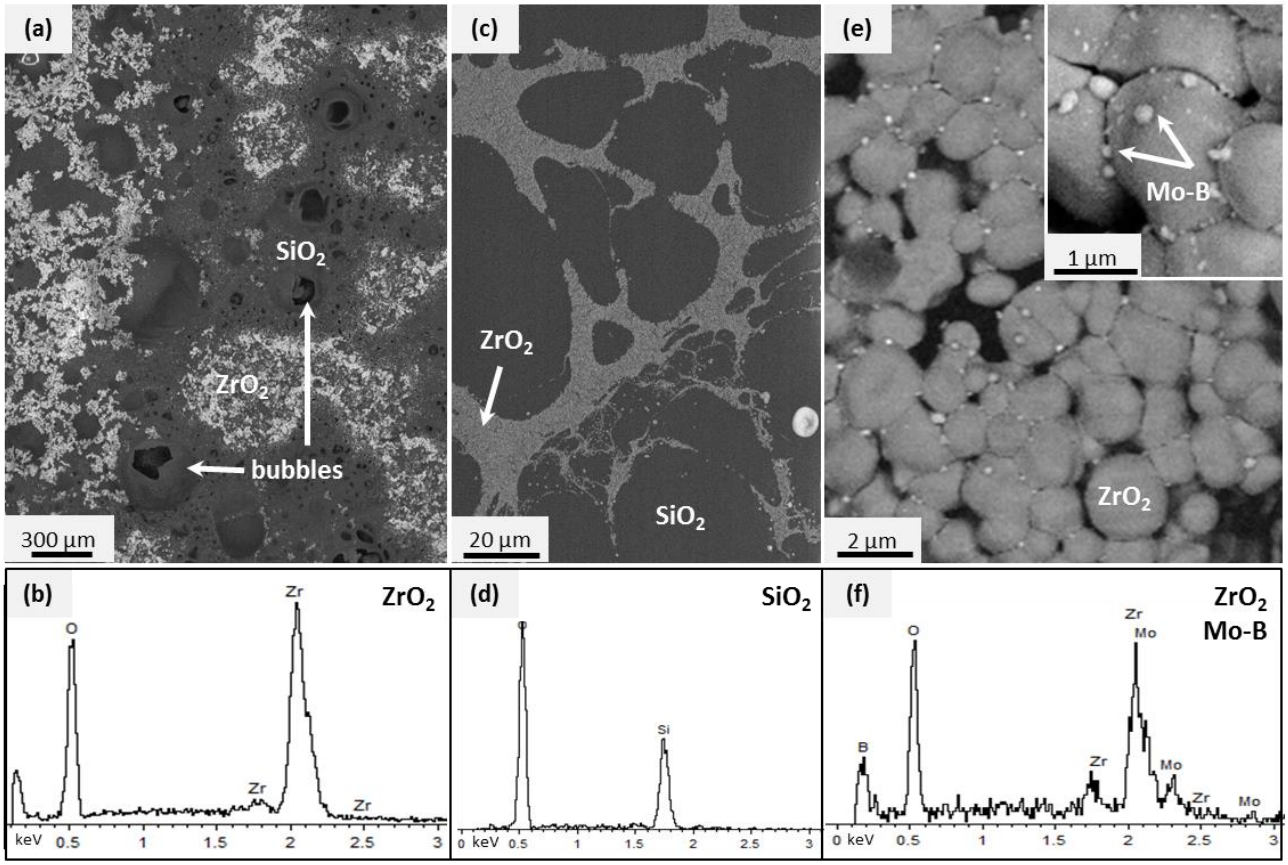

Fig. 5: *a) SEM image of the oxidized surface of material A showing the overall appearence with EDS of pure ZrO_2 in b). c-f) SEM images of the oxidized surface of material B showing the c) overall appearence with SiO_2 glass and crystalline agglomerates and e) magnification of the ZrO_2 precipitates with Mo-B inclusions and d), f) corresponding EDS spectra.*

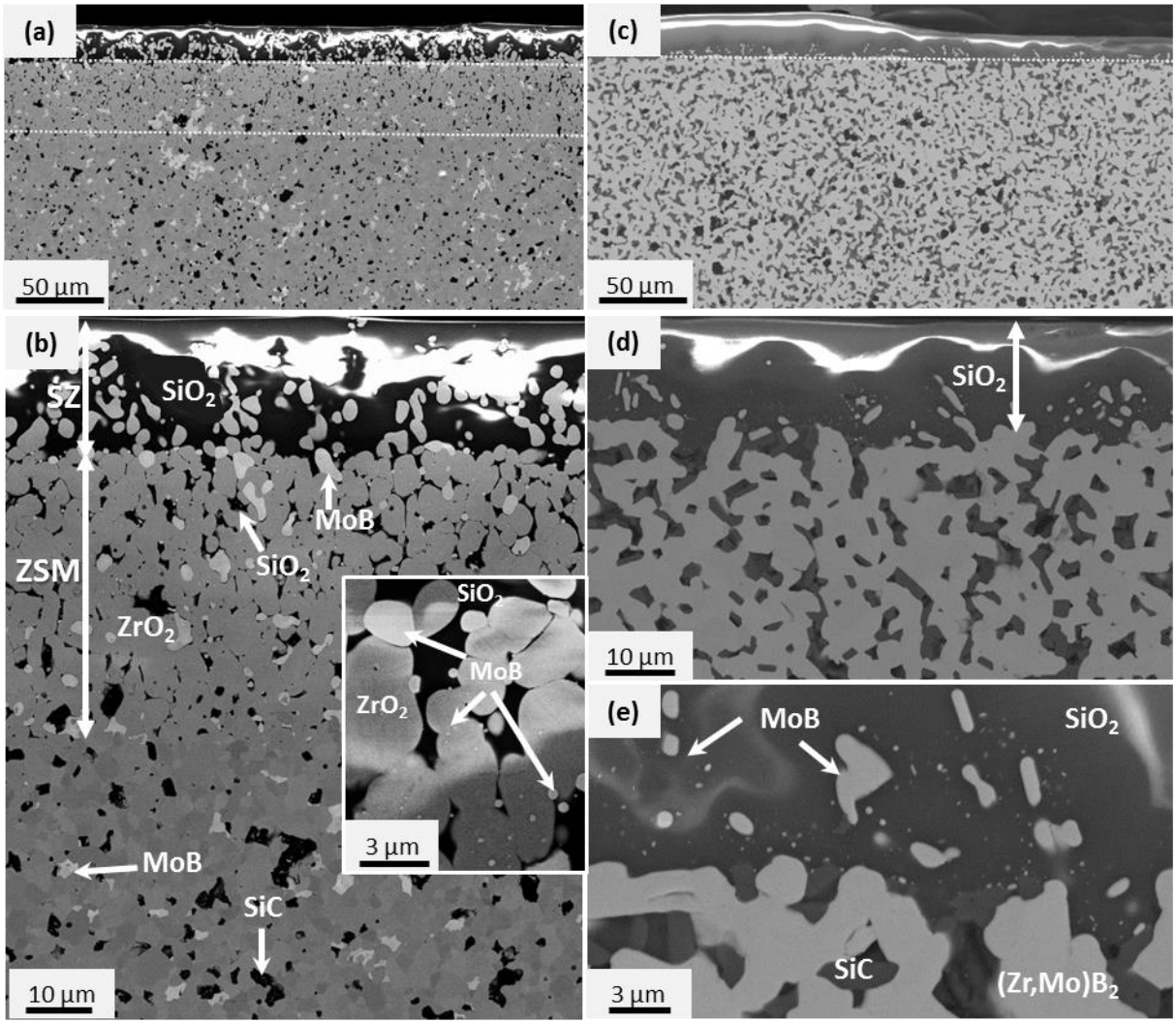

Fig. 6: *SEM images of the oxidized cross sections of materials a)-b) A and c)-e) B showing the different modified thickness and architecture. Tags in b) corresponds to different oxidized layers: SZ - SiO_2 glass embedding ZrO_2 aggregates, ZSM - ZrO_2 encasing $MoSi_2$ oxidation products, MoB and SiO_2. The inset in b) is a magnificatino of the SZ/ZSM interface evidencing bright nano-inclusions within ZrO_2 grains.*

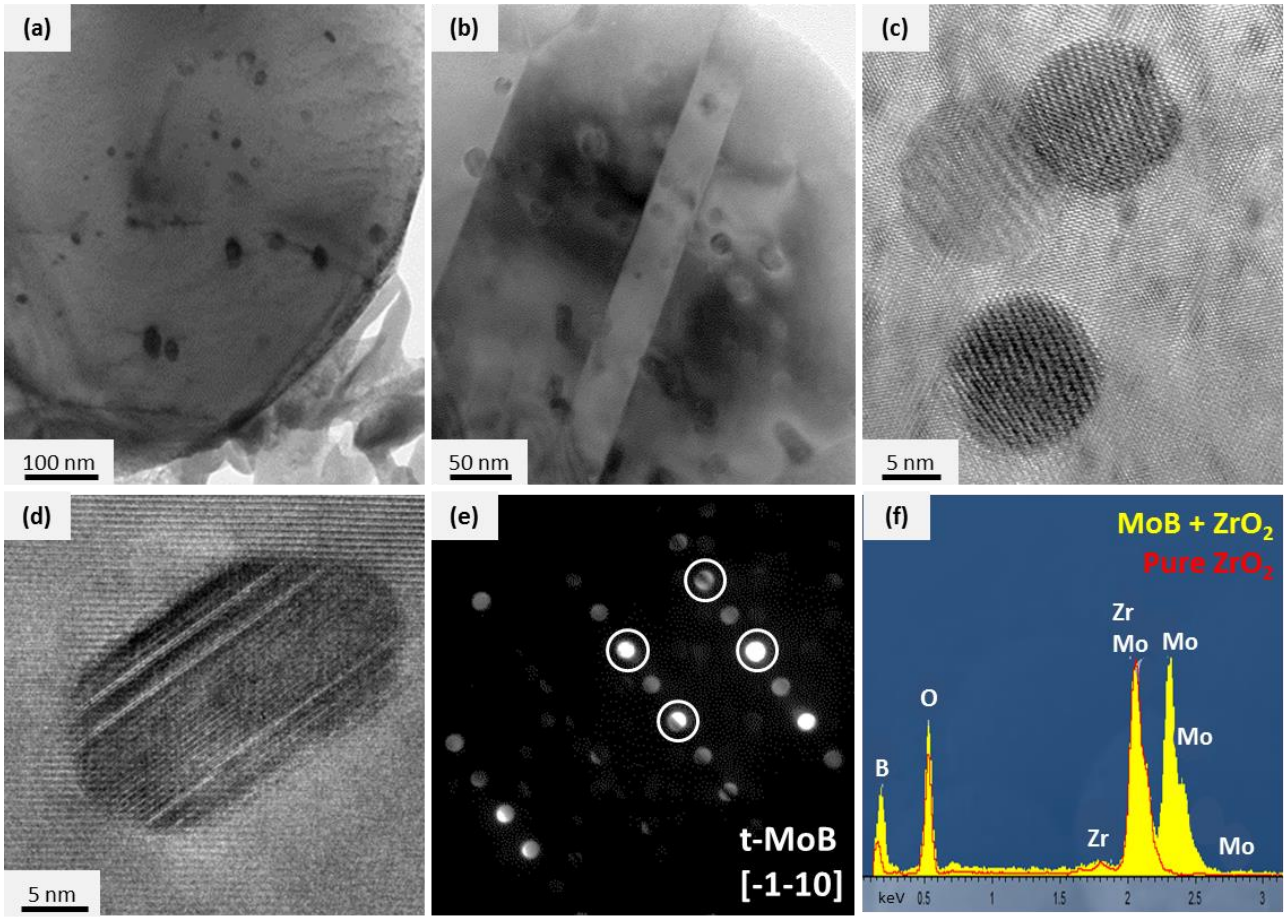

Fig. 7: *TEM images of ZSM layer in material A showing a)-b) the overall appearence of ZrO_2 grains with nestled nano-sized particles, c)-d) HR-TEM of such MoB inclusions, identified by e) diffraction pattern and f) EDS analysis. The spectrum of pure ZrO_2 is shown too, to discriminate the signal relative to MoB phase.*

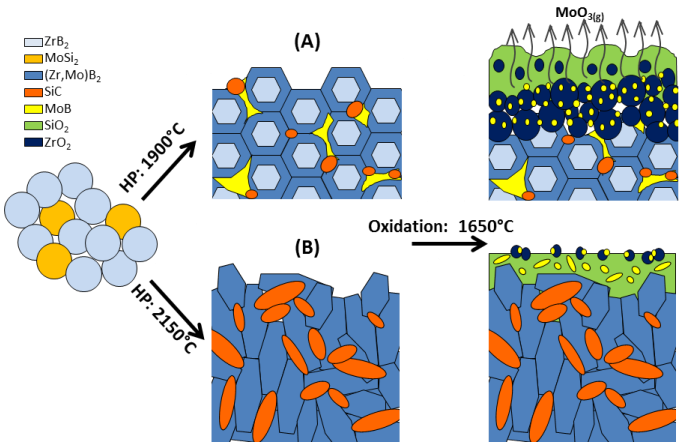

Fig. 8: *Sketch of the different microstructures resulting from different hot pressing temperature and corresponding architecture of the oxidized scales.*

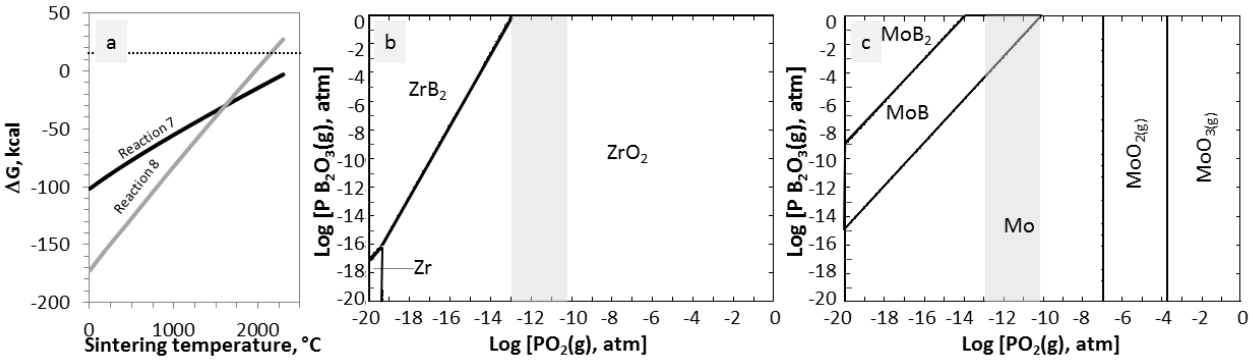

Fig. 9: *a) Free Gibbs energy, ΔG, measured for reactions (7) and (8) as a function of the sintering temperature showing that at high temperature reaction (7) is more favorable. Phase stability diagrams for the b) Zr-B-O and c) Mo-B-O systems as a function of oxygen and boron oxide partial pressures calculated at 1650°C. The shaded areas evidence that the most stable compounds are different in the two systems under the same conditions of temperature and pressure, ZrO_2 versus MoB/Mo.*

Figures captions

Fig. 1: X-ray diffraction patterns of materials A and B showing peaks splitting in the first and peaks shift in the second one. The table inset lists the calculated lattice parameters for the two solid solutions and the amount of Mo dissolved, as estimated from Vegard's rule.

Fig. 2: SEM images showing the microstructure of material A (a-c) and B (d-f).

Fig. 3: a) SEM image showing microstructural details in material A with the corresponding b) EDS spectra of core and rim phases. c) SEM image of material B with elemental distribution of Zr, Mo and Si with d) EDS spectra of the $(Zr,Mo)B_2$ solid solition superimposed to that of pure ZrB_2.

Fig. 4: X-ray diffraction patterns of materials A and B upon cyclic oxidation showing the boride as main phase in the first and the oxide in the second one. The inset shows photos of the ceramics after the 3 oxidation cycles at 1650°C.

Fig. 5: a) SEM image of the oxidized surface of material A showing the overall appearence with EDS of pure ZrO_2 in b). c-f) SEM images of the oxidized surface of material B showing the c) overall appearence with SiO_2 glass and crystalline agglomerates and e) magnification of the ZrO_2 precipitates with Mo-B inclusions and d), f) corresponding EDS spectra.

Fig. 6: SEM images of the oxidized cross sections of materials a)-b) A and c)-e) B showing the different modified thickness and architecture. Tags in b) corresponds to different oxidized layers: *SZ* - SiO_2 glass embedding ZrO_2 aggregates, *ZSM* - ZrO_2 encasing $MoSi_2$ oxidation products, MoB and SiO_2. The inset in b) is a magnificatino of the *SZ/ZSM* interface evidencing bright nano-inclusions within ZrO_2 grains.

Fig. 7: TEM images of *ZSM* layer in material A showing a)-b) the overall appearence of ZrO_2 grains with nestled nano-sized particles, c)-d) HR-TEM of such MoB inclusions, identified by e) diffraction pattern and f) EDS analysis. The spectrum of pure ZrO_2 is shown too, to discriminate the signal relative to MoB phase.

Fig. 8: Sketch of the different microstructures resulting from different hot pressing temperature and corresponding architecture of the oxidized scales.

Fig. 9: a) Free Gibbs energy, ΔG, measured for reactions (7) and (8) as a function of the sintering temperature showing that at high temperature reaction (7) is more favorable. Phase stability diagrams for the b) Zr-B-O and c) Mo-B-O systems as a function of oxygen and boron oxide partial pressures calculated at 1650°C. The shaded areas evidence that the most stable compounds are different in the two systems under the same conditions of temperature and pressure, ZrO_2 versus MoB/Mo.